PHYSICAL REVIEW E **101**, 042101 (2020)

Detecting depinning and nonequilibrium transitions with unsupervised machine learning

D. McDermott,[1,2] C. J. O. Reichhardt,[1] and C. Reichhardt[1]
[1]*Theoretical Division, Los Alamos National Laboratory, Los Alamos, New Mexico 87545, USA*
[2]*Department of Physics, Pacific University, Forest Grove, Oregon 97116, USA*

(Received 3 September 2019; accepted 10 March 2020; published 3 April 2020)

Using numerical simulations of a model disk system, we demonstrate that a machine learning generated order-parameter-like measure can detect depinning transitions and different dynamic flow phases in systems driven far from equilibrium. We specifically consider monodisperse passive disks with short range interactions undergoing a depinning phase transition when driven over quenched disorder. The machine learning derived order-parameter-like measure identifies the depinning transition as well as different dynamical regimes, such as the transition from a flowing liquid to a phase separated liquid-solid state that is not readily distinguished with traditional measures such as velocity-force curves or Voronoi tessellation. The order-parameter-like measure also shows markedly distinct behavior in the limit of high density where jamming effects occur. Our results should be general to the broad class of particle-based systems that exhibit depinning transitions and nonequilibrium phase transitions.

DOI: 10.1103/PhysRevE.101.042101

I. INTRODUCTION

Principal component analysis (PCA) is a linear algebra algorithm that is widely used for identifying patterns in data sets [1]. PCA determines the axes along which a data set has the largest variance by expressing the set as a linear sum of basis vectors. The principal components (PCs) are the eigenvectors of the data matrix eigenvalue, and the first principal eigenvector has the largest possible eigenvalue. PCA is closely related to single vector decomposition, as detailed in Ref. [2], a primer on the mathematics of PCA. Applications of PCA include whitening data and reducing the dimensionality of the system. Often researchers with large data sets use PCA as a tool to reveal a hidden underlying relationship among variables by changing the basis in which the data are expressed and computing the principal components. In reducible data sets, the sum of basis vectors can be truncated while maintaining a reasonable approximation of the original data.

PCA in conjunction with machine learning is used in a broad range of fields where large data sets are common and the underlying relationship between the variables may not be apparent, such as in biology [3,4] and pattern recognition [5]. Use of PCA requires the construction of a feature matrix, where a feature is a general name for a measurement of a system. Typically, the feature matrix contains data trials along its rows, which are often called samples in machine learning, and different features along its columns. For example, in facial recognition applications, the pixel values of a digitized photo are used as features, and each photo is considered a sample. The PCA algorithm fits the data and outputs the principal components written as linear combinations of the original features. The algorithm synthesizes information using minimization techniques that maximize the variance along the principal components, which may result from an underlying fundamental physical model.

In condensed matter physics, PCA has successfully been applied to detect phase transitions in the Ising and XY models based on matrices of raw spin configurations [6–9]. In a detailed study of various spin models, Hu *et al.* [8] confirmed that PCA is well suited for recognizing order and symmetry breaking, and showed that the distribution of principal components can be used to separate strong first order transitions from second order transitions as well as to distinguish phase transitions from pattern changes. Equilibrium phase transitions in a variety of soft matter systems not confined to a lattice can be detected with PCA, such as a density-driven liquid to hexatic phase transition in passive disks [10,11], where PCA was able to reproduce the qualitative shape of the traditional order parameters. In Ref. [11] the method was extended to nonequilibrium phase transitions such as random organization [12]. In these studies, the features are constructed intuitively using measures similar to the pair correlation function $g(r)$, which is known to be an excellent indicator of both short and long range order in tightly packed particle systems. Intriguingly, the transformed principal components found by PCA can be related to the packing structures in the disk systems, and by modifying the sampling of the number of probe particles and neighbor particles, it is possible to develop physical insights regarding the shape and magnitude of an order-parameter-like quantity [11].

Since PCA methods have proven successful at characterizing certain nonequilibrium systems, it is natural to apply these methods in systems that exhibit depinning transitions when individual particles, groups of particles, or elastically coupled elements are driven over quenched disorder [12,13]. Such behavior arises for the depinning of magnetic vortex lines in type-II superconductors [14–18], magnetic domain walls [19], contact lines [20], electron crystals [21–23], stripe and bubble phases, [24–27], sliding quantum crystals [28], skyrmions [29–34], sliding charge density waves [35–37], colloids [38–43], jammed systems with quenched disorder [44,45], sliding friction [46–48], geological systems [49], dislocation dynamics [50,51], pattern forming systems [52], and active matter [53,54]. In addition to the depinning transition, these systems can exhibit a wealth of distinct dynamical flow phases along with transitions between these phases, such as depinning into a disordered liquid [15,17,18,23,25,33,38–40] followed by a transition into a moving crystal [14–16,31,34,35], moving smectic [18,19,25,26,41,42,55–57], or other moving pattern [25,26,51,52,54] at higher drives. Traditional methods to characterize these systems include the velocity-force curves, differential conductivity, structure factor, and Voronoi tessellations [13]; however, there are many cases in which the system exhibits dynamics that appear different to the eye but are not distinct according to these standard measures, Thus, the nature of the appropriate order parameter is often not clear. There have been some studies using machine learning algorithms to detect depinning transitions on ferroelectric relaxors using the k-means algorithm [58]. It is, however, an open question whether a PCA generated order-parameter-like measure can characterize transient and steady state nonequilibrium flow phases, as well as nonequilibrium phase transitions, such as those observed in particle based systems.

In this paper, we apply PCA to driven monodisperse disk systems with quenched disorder. Despite the apparent simplicity of this system, it exhibits not only depinning transitions but also a variety of distinct dynamical phases, including laning, clustering, crystalline, and jammed phases [59]. Often the transitions between these phases only produce weak signatures in the standard measures. We demonstrate that PCA can automatically detect the different dynamic behaviors as a function of drive. The features we employ are constructed from intuitive measures similar to the pair correlation function $g(r)$ used in Jadrich *et al.* [10,11]. We show that the machine learning derived order-parameter-like measure is superior to the standard measures, indicating that combining the pairwise distance information into principal components using PCA can successfully synthesize the fundamental information of the emergent behavior. This method could be applied to a wide variety of other particle-based systems that exhibit depinning.

The paper is organized as follows. In Sec. II we outline the principal component analysis technique for the depinning system. The simulation details of the disk system, along with the standard measures such as the velocity-force curve and Voronoi tessellation are described in Sec. III. We show in Sec. IV that the principal component analysis of the disk system at different densities can identify distinct changes which correlate with changes in the dynamics and structure of the system, and in Sec. V we summarize our results.

II. PRINCIPAL COMPONENT ANALYSIS OF DISK SYSTEMS

PCA is designed to discover and maximize correlations in data sets contained in matrices [8]. The features range from pixel values of the digitized photo in facial recognition applications to the matrix of spin values in spin-based systems. In off-lattice systems, the raw position data do not naturally lend themselves to description by an m by n matrix. Thus to apply PCA to disks, it is useful to apply traditional measures of structural information. Here we use a "particle centered" measure in PCA to perform dimensionality reduction on the geometrical environment of the particles themselves, rather than attempting to classify the manner in which particles fit into the container. We consider a two-dimensional (2D) system of disks of radius r interacting with a random array of pinning sites, as described in [59]; additional simulation details appear in Sec. III.

We characterize the structural information of the disks using the relative positional data, $r_{ij} = |\mathbf{r}_{ij}|$, where $\mathbf{r}_{ij} = \mathbf{r}_i - \mathbf{r}_j$ is the center-to-center distance between disks i and j. For a certain subset of probe particles $m = N_{\text{probe}} = 1000$, we measure the distance from the probe particle to n of its neighbor particles. We sort the resulting distances and place the values into a feature vector for each probe particle i,

$$\vec{f_i} = [r_{i0}, r_{i1}, r_{i2}, \dots, r_{ij}, \dots, r_{\text{in}}]. \tag{1}$$

such that $r_{i0} < r_{i1} < \cdots < r_{\text{in}}$. In a procedure typical for PCA, we center the feature vectors by computing the average of each neighbor distance,

$$\langle r_j \rangle_D = \frac{1}{N_{\text{probe}}} \Sigma_{i=0}^{N_{\text{probe}}} r_{ij}, \tag{2}$$

in order to create a vector containing a series of averages:

$$\langle \vec{r} \rangle_D = [\langle r_0 \rangle_D, \langle r_1 \rangle_D, \dots, \langle r_j \rangle_D, \dots, \langle r_n \rangle_D]. \tag{3}$$

We subtract $\langle \vec{r} \rangle_D$ from each feature vector $\vec{f_i}$.

We assemble the centered feature vectors into a feature matrix:

$$\vec{F} = [\vec{f_0}, \vec{f_1}, \vec{f_2}, \dots, \vec{f_m}]^T. \tag{4}$$

To remove the correlations introduced in the sorting process, we perform the essential step of whitening the data, as in Refs. [10,11]. This is necessary to avoid having the PCA algorithm identify only the sorting-induced correlations instead of the intended structural transitions. The whitening transformation is performed by applying the PCA algorithm to a feature matrix of an ideal gas composed of noninteracting disks at density ϕ using the same number of probe N_{probe} and neighbor n disks as in our actual system. The PCA analysis of the ideal gas system generates a transformation matrix, $\vec{W}_0(\phi)$, that transforms the ideal gas system with density ϕ into a Gaussian distribution with mean zero and variance one. We can then use $\vec{W}_0$ to transform feature matrices from nonideal gas systems with density ϕ into a coordinate space in which naive sorting correlations have been removed, preserving only the features that contain correlations due to the particle interactions and external forces. It is necessary to compute a separate $\vec{W}_0$ for each density ϕ.

To implement PCA, we use the incremental PCA library available through Scikit-Learn [60] in order to process many feature vectors without holding the entire feature matrix in memory. After analyzing the whole data set, the PCA algorithm returns a transformation matrix, $\vec{W}(\phi)$, that can be applied to new data. Here, we generate $\vec{W}$ at fixed density ϕ values for all values of F_D. Thus the algorithm simultaneously "sees" systems above and below the depinning transition in the variety of different phases that are described and plotted in a phase diagram in Ref. [59].

In order to apply the PCA algorithm, we run the disk simulation until the system reaches a steady state. Then we sample snapshots of the system, using 10–50 frames spaced by $\Delta t = 1000$–10^4 simulation time steps. In each frame we randomly select $m = 1000$ probe particles, and for each particle we calculate the distance to its n nearest neighbors. Here we take $n = N_d(\phi) - 1$, where $N_d(\phi)$ is the total number of disks in the sample at density ϕ, meaning that we calculate the distance from the probe particle to all other particles in the system. For each simulation frame we generate the centered feature vector $\vec{f}_i$. This must be prewhitened to obtain $\vec{f}_i^w = \vec{W}_0(\phi)\vec{f}_i$. To generate a PCA transformation matrix $\vec{W}(\phi)$ valid for disk density ϕ, we analyze all feature data from all frames (obtained at all possible values of F_D) for the given disk density ϕ by feeding ten $m \times n$ matrices of prewhitened feature vectors into the incremental PCA algorithm in sequence. The algorithm returns the transformed data $\vec{f}'$, eigenvalues λ_N, and the transformation matrix $\vec{W}$. This matrix may be used to transform new prewhitened feature vectors from subsequent snapshots of data obtained at the same value of ϕ, or it can be applied to the already processed feature vectors in order to generate a visualization of the vectors in the new basis space.

Jadrich and co-workers [10,11] showed that the principal components contain structural information of the system, and thus can be used as an order-parameter-like measure (OP) of the system. To construct such an OP, we transform a prewhitened feature vector $\vec{f}_i^{\,w}$ obtained at fixed F_D and ϕ with the trained PCA model to obtain

$$\vec{p}_i = \vec{W}\vec{f}_i^w. \tag{5}$$

The order-parameter-like measure P_1 is defined to be the extent to which the first principal component captures the information content in the system,

$$P_1 = \langle |p_1| \rangle, \tag{6}$$

where p_1 is the first element in $\vec{p}$. We analyze the eigenvalue spectrum using a scree plot to determine how well the matrix can be expressed in the new PC basis. We also plot the magnitude of the first principal component, the total transformation matrix $\vec{Q} = \vec{W}\vec{W}_0$ that is remarkably similar to $g(r)$, and the machine learning (ML) derived OP $P_1 = \langle |p_1| \rangle$.

III. SIMULATION AND SYSTEM

We analyze the data from our previous publication [59], in which we performed 2D molecular dynamics simulations of passive disk systems. The system contains N_d disks of radius R_d within a simulation box of $S_x = S_y = 60.0$, in dimensionless simulation length units, with periodic boundary conditions. The area density is given by $\phi = N_d\pi R_d^2/(S_xS_y)$. In the absence of quenched disorder, the disks form a polycrystalline state near $\phi \approx 0.85$ and a triangular solid at $\phi \approx 0.9$.

The disk dynamics are governed by the following overdamped equation of motion:

$$\eta\frac{d\mathbf{r}_i}{dt} = \mathbf{F}_{dd} + \mathbf{F}_p + \mathbf{F}_D. \tag{7}$$

Here η is the damping constant and $\mathbf{r}_i$ is the location of disk i. The disk-disk interaction force is $\mathbf{F}_{dd} = \sum_{i\neq j} k(2R_d - |\mathbf{r}_{ij}|)\Theta(2R_d - |\mathbf{r}_{ij}|)\hat{\mathbf{r}}_{ij}$, where $\mathbf{r}_{ij} = \mathbf{r}_i - \mathbf{r}_j$, $\hat{\mathbf{r}}_{ij} = \mathbf{r}_{ij}/|\mathbf{r}_{ij}|$, the disk radius $R_d = 0.5$, and the spring constant $k = 50$. Distances are measured in simulation units l_0 and forces are measured in simulation units f_0 so that k is in units of f_0/l_0 and the unit of simulation time is $\tau = \eta l_0/f_0$.

We introduce quenched disorder by placing pinning sites throughout the sample. The pinning force $\mathbf{F}_p$ is modeled as arising from N_p randomly placed parabolic attractive wells with a pinning radius of $r_p = 0.5$, such that only a single disk can be trapped in a given pinning site at any given time. We fix the pinning density to $\phi_p = N_p/(S_xS_y) = 0.314$. The driving force $\mathbf{F}_D = F_D\hat{\mathbf{x}}$ is applied uniformly to all particles and is incremented in steps of $\Delta F_D = 0.05$ after every $\Delta t = 1 \times 10^6$ simulation time steps. We initialize the disks in random nonoverlapping positions and allow the system to reach a steady state at each drive by waiting 10^6 simulation time steps before obtaining data.

At each drive increment, we measure the average disk velocity $\langle V_x \rangle = N_d^{-1}\sum_{i=1}^{N_d}\mathbf{v}_i\cdot\hat{\mathbf{x}}$, where $\mathbf{v}_i$ is the instantaneous velocity of disk i. The system is completely athermal but the disks experience fluctuations due to the combination of the driving force, the pinning sites, and neighboring disks.

A useful measure for characterizing interacting particles driven over disorder is the fraction P_6 of sixfold-coordinated particles. Here $P_6 = N_d^{-1}\sum_i^{N_d}\delta(z_i - 6)$, where z_i is the coordination number of disk i obtained from a Voronoi tessellation. Previously [59], we correlated local maxima in P_6 with changes in the dynamic phases, and demonstrated that P_6 did not have a feature at all of the dynamical phase transitions. This behavior for the disks with short range interactions differs from what is observed for particles that have longer range interactions, where the dynamic phase changes are more readily detected using information from the Voronoi tessellation.

IV. RESULTS

In Fig. 1 we plot the traditional dynamical measurements as a function of F_D/F_p for a sample with fixed pinning density at different disk densities ϕ ranging from $\phi = 0.25$ to $\phi = 0.85$. The velocity-force curves $\langle V_x \rangle$ versus F_D/F_p in Fig. 1(a) have the same features that are generically found in systems that undergo depinning. At low drive, there is a pinned regime with $\langle V_x \rangle = 0$. This is followed at higher drive by a nonlinear regime above depinning, and at the highest drives, there is a regime in which the velocity increases linearly with increasing F_D. As the disk density increases, the depinning transition shifts to lower F_D and the region of nonlinear velocity response becomes narrower. In Fig. 1(b), the fraction P_6 of sixfold coordinated disks versus F_D/F_p is nearly flat for $\phi = 0.25$ and 0.3, while for higher ϕ there is some tendency for P_6 to increase with increasing F_D. Overall, the results in Fig. 1 indicate that it is difficult to identify distinct dynamic phases using these measures, and that it is even difficult to precisely pinpoint the depinning transition.

A. Low disk density

We first focus on the low density limit with $\phi = 0.25$ and $\phi = 0.3$, where P_6 is almost featureless. In Fig. 2 we illustrate the disk configurations in a sample with $\phi = 0.3$ at different values of F_D/F_p. In the pinned phase at $F_D/F_p = 0.25$, Fig. 2(a) shows that small disordered clusters appear

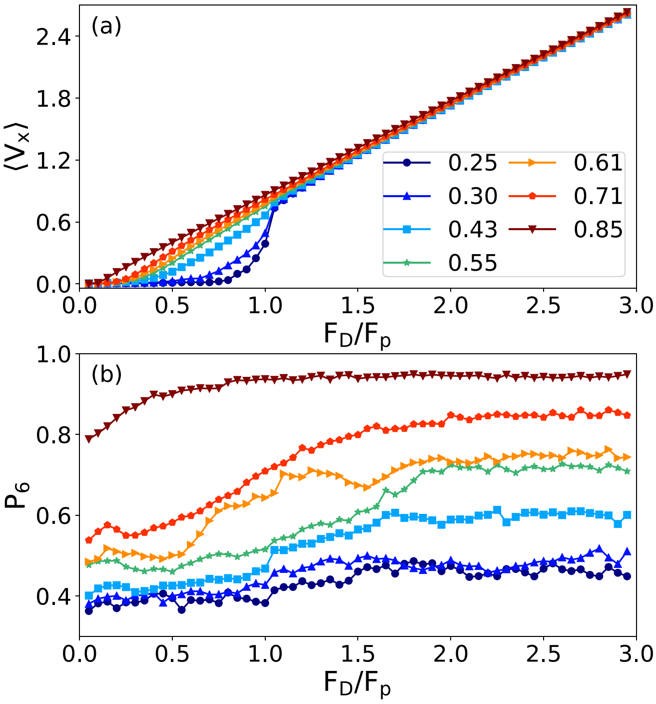

FIG. 1. (a) The average disk velocity $\langle V_x \rangle$ vs driving force F_D/F_p in samples with total disk density ϕ of $\phi = 0.85$ (down triangles), 0.71 (pentagons), 0.61 (right triangles), 0.55 (stars), 0.43 (squares), 0.30 (up triangles), and 0.25 (circles). (b) The corresponding P_6 vs F_D/F_p.

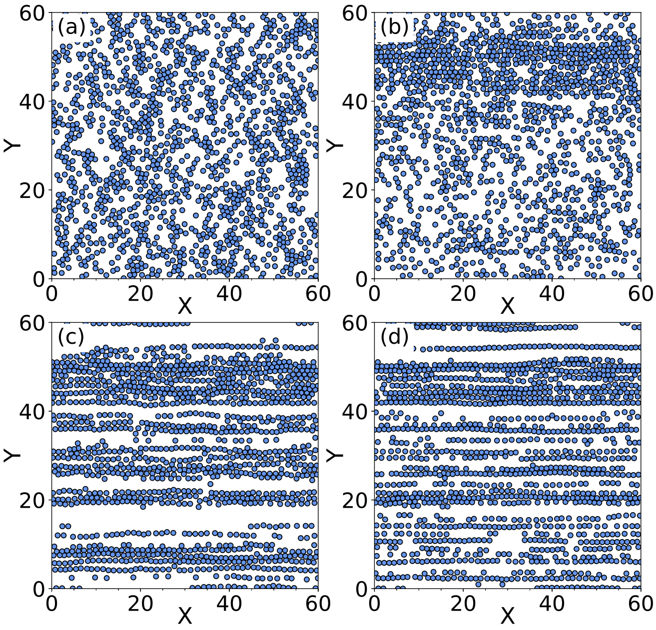

FIG. 2. Images obtained at a disk density of $\phi = 0.30$ for the system in Fig. 1 at $F_D = 0.25$ (pinned), (b) $F_D = 0.95$ (phase separated), (c) $F_D = 1.5$ (smectic flow), and (d) $F_D = 2.5$ (smectic flow).

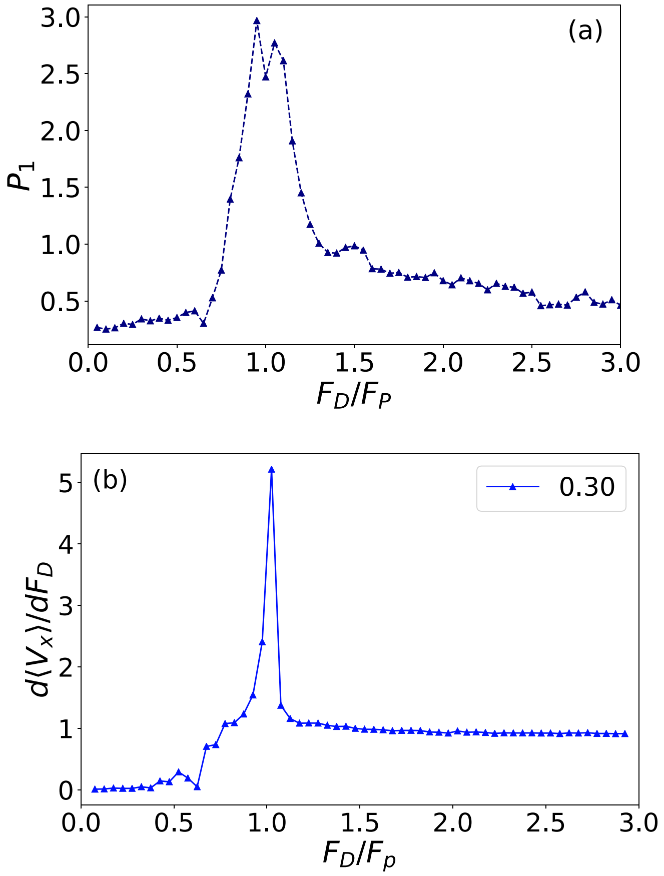

FIG. 3. (a) The machine learning derived order-parameter-like measure P_1 vs F_D/F_p for the system in Fig. 1 at disk density $\phi = 0.30$ with 50 realizations. Three phases are clearly apparent: the pinned state at $0 < F_D/F_p < 0.65$, the phase separated state at $0.65 \leqslant F_D/F_p < 1.3$, and the smectic or laned state at $F_D \geqslant 1.3$. (b) $d\langle V_x \rangle / dF_D$ vs F_D/F_p for the same system.

since some of the particles have formed clogged clusters instead of being directly trapped by the pinning sites. Above depinning at $F_D/F_p = 0.95$ in Fig. 2(b), there is a combination of smaller pinned clusters with a phase separated region of higher density in which the disks move in a band. In Fig. 2(c) at $F_D/F_p = 1.5$, all the disks are moving in one-dimensional (1D) chains, while in Fig. 2(d) at $F_D = 2.5$, the moving chains have become somewhat more rarefied. These results indicate that different dynamical regimes are present which are generally not detectable with the standard measures. We note that other measures such as the structure factor $S(k)$ and diffusion similarly show only weak or no changes at the transitions among these dynamical regimes.

In Fig. 3 we plot the machine learning derived OP P_1 versus F_D/F_p for the system in Fig. 1. We find $P_1 \approx 0.25$ for $0 < F_D/F_p < 0.65$, which is the pinned state illustrated in Fig. 2(a). This is followed by an increase in P_1 at $F_D/F_p = 0.65$, corresponding to the depinning transition. P_1 remains elevated over the range $0.65 \leqslant F_D/F_p < 1.05$ in the phase separated state shown in Fig. 2(b). For $1.05 \leqslant F_D/F_p < 1.4$, P_1 decreases when the system crosses over into the smectic or laned state. A small local maximum in P_1 occurs around $F_D/F_p = 1.50$ where the laned particles form the widest horizontal bands, such as the band appearing between $35 < y < 55$ in Fig. 2(c). There is a gradual decrease in P_1 from $P_1 \approx 1.0$ to $P_1 \approx 0.5$ over the range $1.6 \leqslant F_D/F_p \leqslant 3.0$ as the smectic lanes become increasingly well defined, as shown in Figs. 2(c)

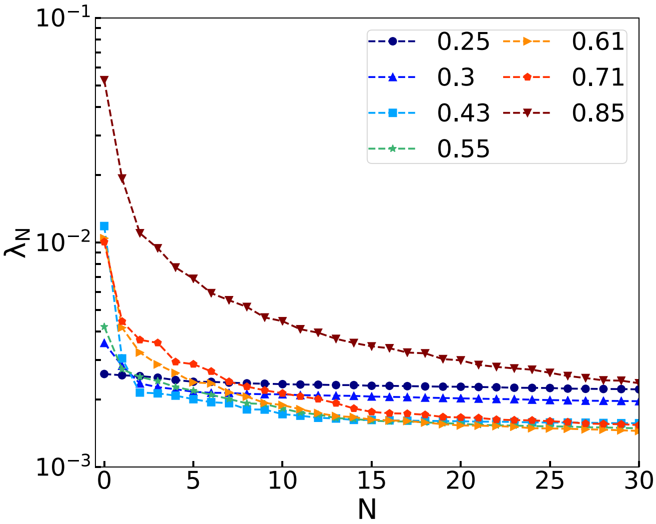

FIG. 4. The scaled eigenvalues (relative scores) λ_N of the PCA algorithm vs the relative ranking N for disk densities of $\phi = 0.85$ (down triangles), 0.71 (pentagons), 0.61 (right triangles), 0.55 (stars), 0.43 (squares), 0.30 (up triangles), and 0.25 (circles). $N = 1$ corresponds to the first principal component.

and 2(d) at $F_D/F_p = 1.5$ and $F_D/F_D = 2.5$. The results in Fig. 3 indicate that P_1 clearly detects and distinguishes the three phases, pinned, phase separated, and smectic, along with the transitions between these states. For $\phi = 0.25$ (not shown), we find similar phases and a similar response of P_1. In Fig. 3(b) we show the derivative $d\langle V_x\rangle/dF_D$ vs F_D/F_p of the quantity $\langle V_x\rangle$ plotted in Fig. 1(a) for $\phi = 0.3$. Distinct features in $d\langle V_x\rangle/dF_D$ are associated with the phase transitions described above. Starting from a value of zero at low F_D/F_p where the system is pinned, $d\langle V_x\rangle/dF_D$ becomes nonzero near $F_D/F_p = 0.65$ at the depinning transition, peaks sharply at $F_D/F_p = 1.0$, and flattens at high driving forces.

B. Eigenvalue distribution

In Fig. 4 we show a scree plot of the eigenvalues λ_N for the samples in Fig. 1 with disk densities of $\phi = 0.25$ to $\phi = 0.85$. Here the eigenvalues are sorted from largest ($N = 1$) to smallest and plotted versus eigenvalue ranking N. The scree plot gives an indication of how successfully the PCA has reduced the dimensionality of the information present in the system. When the eigenvalue spectrum is dominated by one or a few large values of low rank, followed by many small values, it indicates that the first few eigenvectors can be used to describe the primary characteristics of the system, since a linear combination of the first few principal components captures most of the information. At $\phi = 0.25$ and $\phi = 0.3$, the first eigenvalue λ_1 is somewhat larger in size and the remainder of the eigenvalues are nearly flat. For $\phi = 0.3$, we find that λ_2 is 40% smaller than λ_1. At intermediate disk densities of $\phi = 0.43$ to $\phi = 0.71$, λ_1 is substantially larger than the remaining eigenvalues, indicating that the PCA analysis has captured the features of the system well. We find a significant jump up in all the eigenvalues at the high density of $\phi = 0.85$, which corresponds to the onset of jamming behavior.

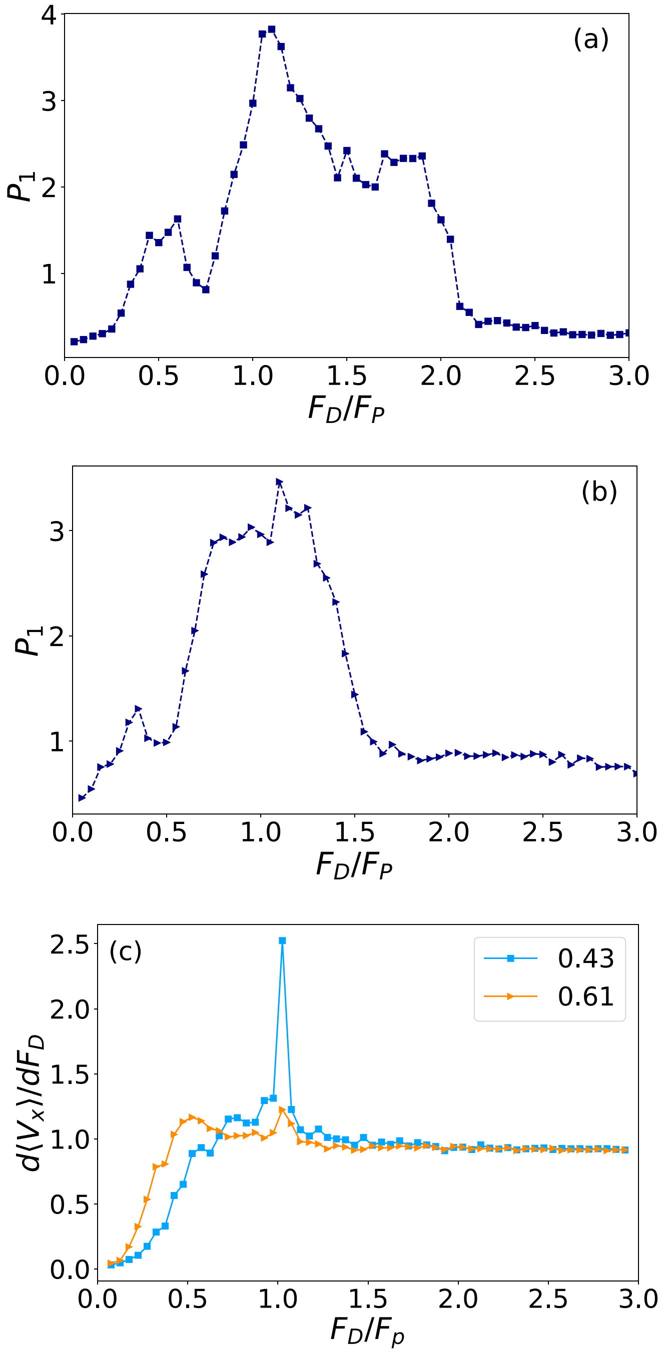

FIG. 5. P_1 vs F_D/F_p for the system in Fig. 1 at intermediate disk densities using 50 realizations. (a) At $\phi = 0.43$, there are multiple peaks. (b) At $\phi = 0.61$, the peak structure is more compressed. (c) $d\langle V_x\rangle/F_D$ vs F_D/F_p for the same systems at $\phi = 0.43$ (blue squares) and $\phi = 0.61$ (orange triangles).

C. Intermediate disk densities

We next consider the intermediate disk density regime. In Figs. 5(a) and 5(b) we plot P_1 versus F_D/F_p for the samples from Fig. 1 with $\phi = 0.43$ and $\phi = 0.61$, respectively. At both densities, in Fig. 1 $\langle V_x\rangle$ versus F_D/F_p is fairly smooth and P_6 has a gradual increase, but it is difficult to distinguish different phases from these measures. In Fig. 5(c) we plot $d\langle V_x\rangle/F_D$ versus F_D/F_p for $\phi = 0.43$ and $\phi = 0.61$. Each

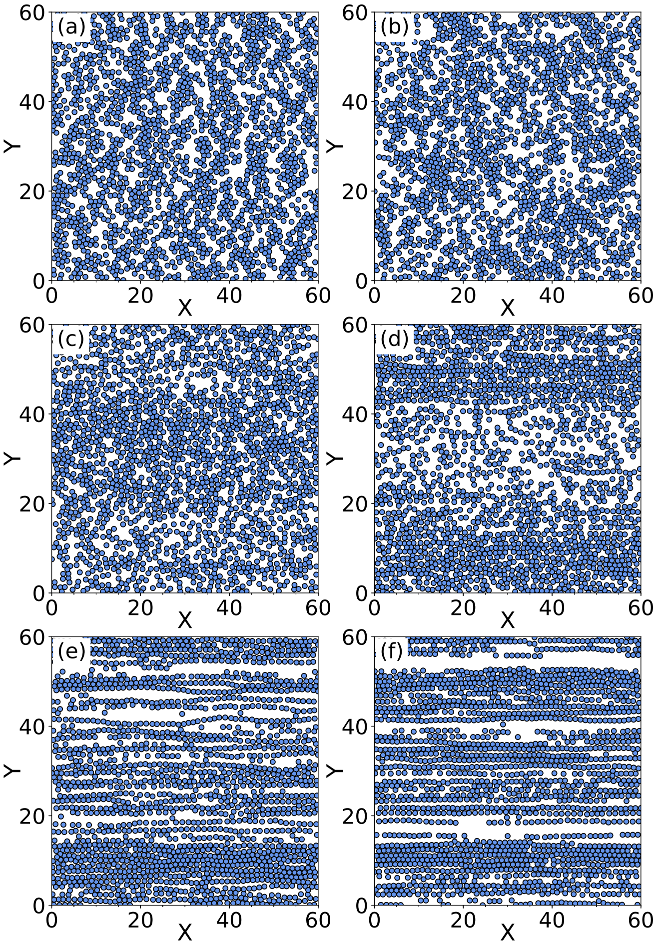

FIG. 6. Images obtained at a disk density of $\phi = 0.43$ for the system in Fig. 5(a) at (a) $F_D/F_p = 0.05$ (disordered pinned state), (b) $F_D/F_p = 0.55$ (clustering clogged state), (c) $F_D/F_p = 0.75$ (moving liquid), (d) $F_D/F_p = 0.95$ (phase separated state with amorphous order), (e) $F_D/F_p = 1.5$ (phase separated state with crystalline order), and (f) $F_D/F_p = 2.5$ (moving smectic).

curve smoothly increases over the range $0 < F_D/F_p < 0.5$ and has a small local maximum near the depinning point. A spike in $d\langle V_x\rangle/F_D$ appears at $F_D/F_p = 1.0$, while at higher drives where the force-velocity curve in Fig. 1 is linear, $d\langle V_x\rangle/F_D$ is flat. In contrast, P_1 in Fig. 5(a) has two clear peaks at $F_D/F_p = 0.55$ and $F_D/F_p = 1.0$, a plateau region over the range $1.5 < F_D < 2.0$, and drops to a low value for $F_D > 2.0$. For $\phi = 0.43$, as shown in Fig. 4 we find that λ_2 is 70% smaller than λ_1, which is the largest difference we observe between λ_1 and λ_2. In Fig. 6(a) we illustrate the disk configuration at $F_D/F_p = 0.05$ within the pinned phase, where P_1 in Fig. 5(a) is small. Here the disks form small clusters in the pinned state. At $F_D/F_p = 0.55$ in Fig. 6(b), just below the depinning transition, the disks form a locally clustered or clogged state, and at depinning these clusters partially break apart, producing the dip in P_1 found in Fig. 5(a). A local minimum in P_1 appears near $F_D/F_p = 0.75$, where the structure is a moving liquid as shown in Fig. 6(c). The amorphous phase separated state at $F_D/F_p = 0.95$ is illustrated in Fig. 6(d). At $F_D/F_p = 1.5$, the system is still phase separated but the amount of crystalline ordering has increased. In Fig. 6(f) the configuration at $F_D/F_p = 2.5$ indicates that the disks have formed a moving smectic state. In general, P_1 shows a pronounced drop at the transition into the moving smectic states, while the corresponding P_6 curve for $\phi = 0.43$ in Fig. 1 exhibits no feature near $F_D/F_p = 2.5$. This indicates that P_1 is much more sensitive to the changes in the disk configurations than P_6 or $\langle V_x\rangle$.

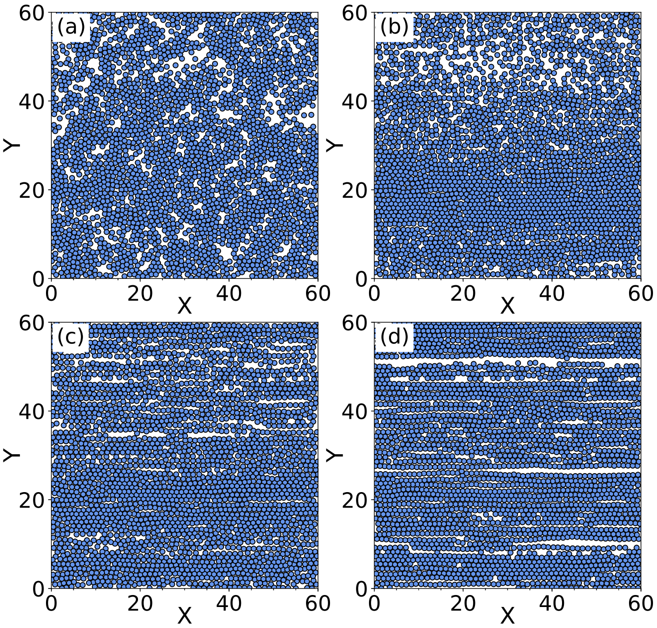

FIG. 7. Images obtained at a disk density of $\phi = 0.61$ for the system in Fig. 5(b) at (a) $F_D/F_p = 0.25$ (pinned clogged state), (b) $F_D/F_p = 0.95$, (phase separated with crystalline order), (c) $F_D/F_p = 1.5$ (moving state), and (d) $F_D/F_p = 2.5$ (moving state).

For $\phi = 0.61$, in Fig. 5(b) P_1 versus F_D/F_p has a trend similar to that found for $\phi = 0.43$. There are some differences, however; the plateau region in P_1 is smaller for $\phi = 0.61$ and the drop in P_1 has shifted to a lower value of $F_D/F_p = 1.5$. Here λ_2 is 60% smaller than λ_1 in Fig. 4. In Fig. 7(a) we illustrate the disk configuration for the $\phi = 0.61$ system at $F_D/F_p = 0.25$, where a pinned clogged state appears. This is the same value of F_D/F_p at which there is a local peak in P_1. Figure 7(b) shows the disk configuration at $F_D/F_p = 0.95$, where the system forms a phase separated state with local crystalline ordering. Here $P_1 = 3.5$, which is close to the same value found for P_1 in the $\phi = 0.43$ sample in the phase separated moving crystal phase illustrated in Fig. 6(e) at $F_D/F_p = 1.5$. Thus, at $\phi = 0.61$, the moving phase separated amorphous state found at lower ϕ is missing. In Fig. 7(c) we show the disk configuration at $F_D = 1.5$, where the local phase separation is reduced and the system begins to form a moving state. This moving state becomes more pronounced in Fig. 7(d) at $F_D = 2.5$.

D. High disk densities

For the lower and intermediate disk densities, there are clear changes in the particle configurations as a function of drive. At high densities of $\phi \geqslant 0.85$, however, the system becomes a uniform jammed solid and the depinning transition

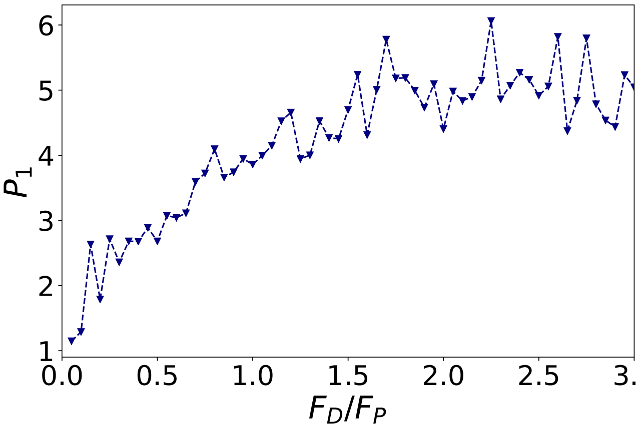

FIG. 8. P_1 vs F_D/F_p for the system in Fig. 1 at $\phi = 0.85$ using 50 realizations, where the disks exhibit jamming behavior and elastic depinning.

changes in character from plastic, where there can be a coexistence of pinned and moving particles, to elastic, where all the particles keep the same neighbors as they move. There is a distinct change in the eigenvalue distribution in Fig. 4 for $\phi = 0.85$, with significant weight appearing at higher values of N, indicating a change in the ability of the PC to capture the information in the system. In Fig. 8 we plot P_1 versus F_D/F_P for $\phi = 0.85$, where λ_2 is 60% smaller than λ_1. Instead of peaks, we find a monotonic increase in P_1 with increasing F_D/F_P. At this density, $d\langle V_x\rangle/dF_D$ vs F_D/F_p (not shown) is nearly flat, as indicated by the constant slope in Fig. 1(a). We find significantly more noise in P_1 at $\phi = 0.85$ than at lower values of ϕ because the local disk density is uniform for all values of F_D/F_P. As a result, there is less natural variance in the system, making it difficult for PCA to discriminate between the nearly identical feature vectors at different values of F_D. In contrast, at lower ϕ the inhomogeneous disk density produces characteristic gaps in the feature vectors, generating relatively high variance in the measured neighbor distances. In Fig. 9(a) we illustrate the disk configuration at $F_D/F_P = 0.25$, where the system forms a mostly triangular solid with a small number of vacancies. For $F_D/F_p = 2.5$, shown in Fig. 9(b), the structure is similar but the amount of triangular order is larger. Here the lack of jumps in P_1 is consistent with the fact that the depinning is elastic and the sample shows no large scale changes in the particle configurations.

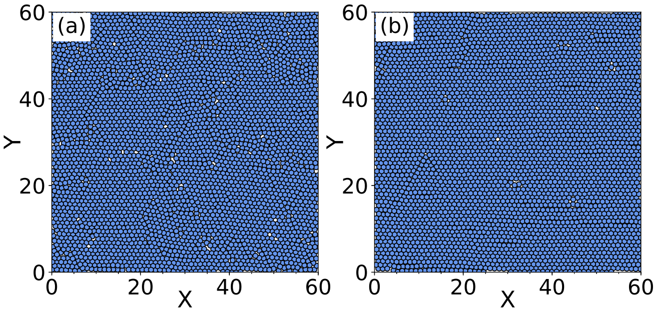

FIG. 9. Images obtained at a disk density of $\phi = 0.85$ for the system in Fig. 8, where the system forms a jammed solid with increasing triangular ordering at higher drives. (a) $F_D/F_p = 0.25$. (b) $F_D/F_p = 2.5$.

E. Properties of the total transformation matrix

The total transformation matrix $\vec{Q} = \vec{W}\vec{W}_0$ provides a physical snapshot of the system not unlike that given by $g(r)$ [10,11]. When applied to a raw feature vector $\vec{f}_i$, $\vec{Q}$ first prewhitens the vector through the $\vec{W}_0$ matrix, and then transforms the vector into the PC basis through the $\vec{W}$ matrix. The first row of Q, termed $[q_1]$, is a convolution of the prewhitening transformation and the basis transformation for the first principal component, such that the expression $p_1 = [q_1]\vec{f}_i$ gives the mapping of the raw feature vector onto the first principal component. The kth component of $[q_1]$ provides the mapping of the kth component of $\vec{f}_i$, and since the elements of $\vec{f}_i$ are ordered according to neighbor distance, with the smallest values of k corresponding to the smallest neighbor distances, it is possible to interpret k as a neighbor distance. The prewhitening portion of $[q_1]$, plotted as a function of k, contains information similar to that found in $g(r)$ of an ideal gas at density ϕ. The transforming portion of $[q_1]$ indicates which neighbor distances are most strongly weighted in the first principal component basis. In Fig. 10 we plot $[q_1]$ versus k from a PCA analysis of the monodisperse passive disks at disk densities of $\phi = 0.25$, 0.43, 0.61, and 0.85. The prewhitening component produces regular oscillations in $[q_1]$ at spacings corresponding to the average distance between successive rings of particles surrounding the probe particle. In an ideal gas, these oscillations would diminish with increasing k. The uneven weighting of the oscillations is an indication of which distance scales are important at each density in the first principal component. In Figs. 10(a)–10(c), samples with low and intermediate densities of $\phi = 0.25$, $\phi = 0.43$, and $\phi = 0.61$ have large peaks of $[q_1]$ at smaller k, indicating that the structural ordering is relatively short ranged. In contrast, the high density $\phi = 0.85$ sample in Fig. 10(d) has strong weightings at much larger k, indicating the long range nature of the emerging crystalline ordering in the jammed state.

Since PCA can identify a structure in the feature vectors that resembles $g(r)$, it can find shells of nearest neighbor distances. PCA differs from the standard structure factor measurement since it associates a single number, P_1 with the *ability* of a $g(r)$-like measure to describe the system. This number can be compared as a scalar quantity across different values of F_D regardless of which wave numbers are dominating the $g(r)$-like measure for any given drive. In contrast, with a measure such as the structure factor, a scalar quantity can be constructed using the weight at a particular wave number, but if the underlying pattern shifts among different wave numbers as a function of drive, this measurement may be quite noisy. The P_1 produced by PCA provides a cleaner signature.

F. Finite size

To check for finite size effects, we analyzed the $\phi = 0.30$ system for samples of size $S_x = S_y = 20$, 40, 60, and 80. We plot P_1 versus F_D/F_p for the different system sizes in Fig. 11, while the $\langle V_x\rangle$ versus F_D/F_p curves for all values of S_x are identical to the curve shown in Fig. 1. In the smallest system

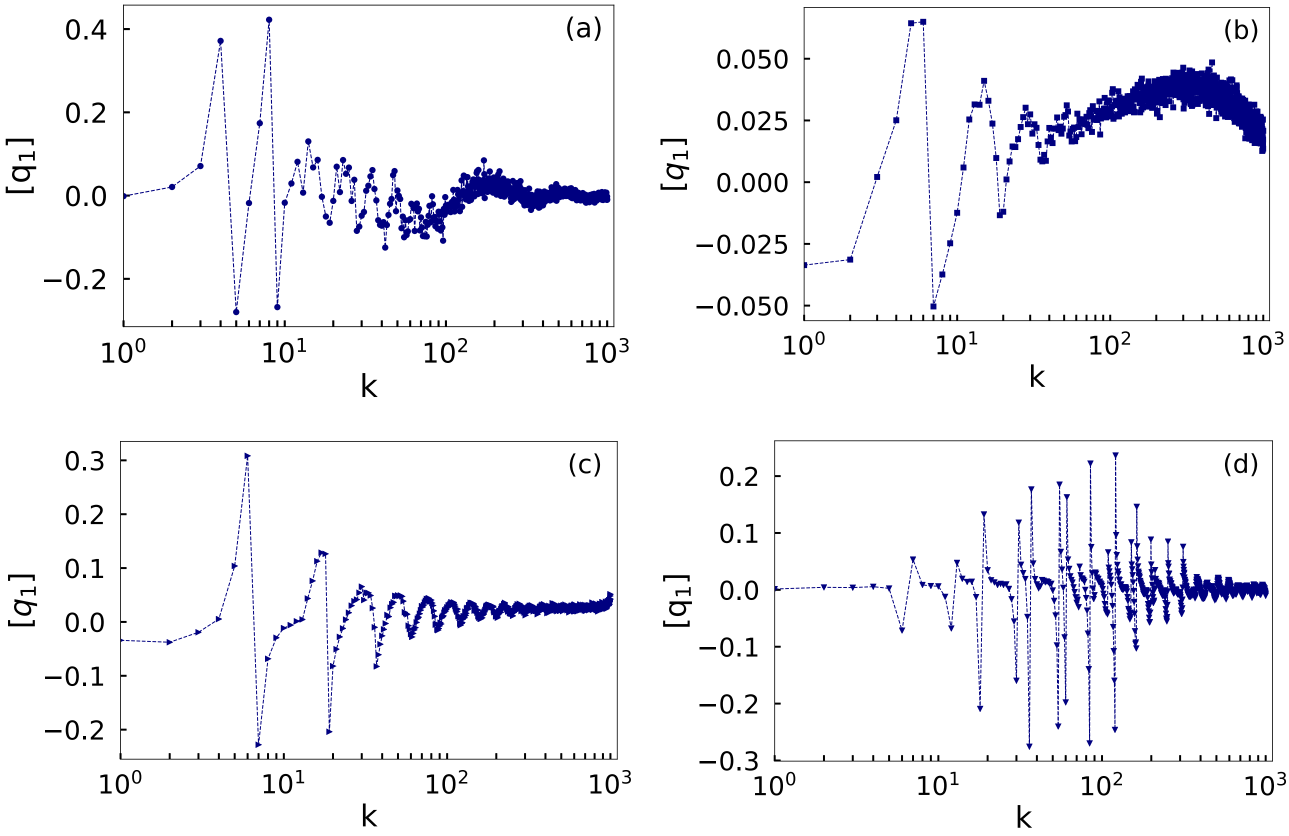

FIG. 10. First vector $[q_1]$ from the total transformation matrix $\vec{Q}$ obtained from 50 realizations versus k, which is related to a neighbor distance, for the system in Fig. 1 at disk densities ϕ = (a) 0.25, (b) 0.43, (c) 0.61, and (d) 0.85.

with $S_X = 20$, the signal in P_1 is lost, but for all of the other system sizes there is a clear signature of the different dynamic phases. The $S_x = 40$ sample is large enough to generate a peak in P_1 near $F_D/F_p = 1$, and this peak becomes sharper in the $S_x = 60$ sample. The peak height diminishes again in the $S_x = 80$ sample due to the fact that we ran all of the systems for 10^6 simulation time steps before measuring, and this was long enough for the smaller samples to reach a full steady state but not for the $S_x = 80$ sample. As a result, the peak height in P_1 is reduced in the $S_x = 80$ sample. At the peak in P_1, a phase separated region forms, and the size of the phase separated cluster compared to the overall number of particles varies with the system size for the same simulation time. All of the curves are similar for $2 < F_D/F_p < 3$, where a laned state appears. In the larger systems, we also tested the effect of varying the number of probe particles as in Ref. [11], reducing this number from the original $m = 1000$ to only $m = 150$. We find that the qualitative shape of P_1 is unchanged even when the number of probe particles is relatively small, which is advantageous since the calculations can be performed more quickly for small m.

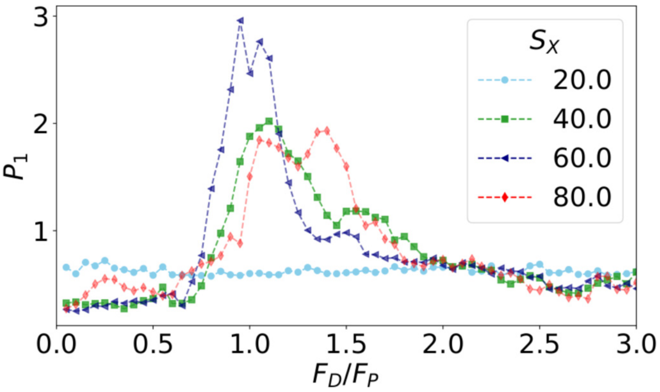

FIG. 11. Finite size analysis of density $\phi = 0.30$ for system of varying sizes. P_1 vs F_D/F_p for $S_x = 20$ (light blue circles), 40 (green squares), 60 (dark blue triangles), and 80 (red diamonds).

V. DISCUSSION

We have demonstrated that unsupervised machine learning can detect depinning and the transitions between different dynamical phases in driven systems with quenched disorder. A similar approach could be adapted for systems with longer range particle-particle interactions, such as superconducting vortices [15,17,18], charged colloids, and Wigner crystals [22,23], which can exhibit a pinned phase, plastic depinning, disordered liquid flow, and a moving crystal or smectic flow phase. In these systems it is often possible to use P_6 to detect the transitions; however, in some situations, additional transitions could be present that produce no signal in P_6 but that could be detected using PCA. For example, at a transition from a liquid to a strongly nematic or smectic state, the density of defects in the lattice undergoes little change and therefore the value of P_6 is constant across the transition, but the PCA could detect the structural change occurring in the system. Additionally, the plastic flow state may be composed of distinct plastic flow phases that have not yet been characterized but that may be detectable using the PCA approach. Depinning of particles on periodic substrates would also be interesting to study since in this system, different types of soliton or incommensurate flow patterns arise. These flow states can often be observed through features in the velocity-force curves, but produce little change in the structure of the particles [16,41–43]. Here, PCA could be applied to more readily distinguish between the different types of commensurate and incommensurate flows.

At high drives, the fluctuations experienced by the disks as they move over the quenched disorder can be described by a shaking temperature T_{sh} of the type introduced in Ref. [15], $T_{sh} \propto 1/F_D$. In Ref. [59] we measured the transverse diffusion of the driven disks, which can be regarded as an estimate of T_{sh}, and found a crossover from subdiffusive to superdiffusive motion at key structural transitions such as the phase segregated state with crystalline order shown in Fig. 7(b). The peaks in P_1 appear at the same transition points.

The spatial Fourier transform of the velocity distribution would be an interesting quantity to consider in future work on a larger system to see whether it matches the behavior of the PCA order-parameter-like measure. In addition, application of PCA to the static phases of a high density system, including some that are purely crystalline, and other systems containing dislocations and/or vacancies, could give an indication of whether PCA is capable of resolving structure at the individual dislocation level or whether it is instead primarily picking up larger scale density heterogeneities. We have tested feature vectors composed of various combinations of V_x, P_4, P_5, P_6, P_7, and the average cluster size, and find that for this system, the nearest neighbor distances provide the most informative feature vector.

PCA could also be applied to the class of systems that exhibit elastic depinning, in which the particles maintain the same neighbors as they begin to flow [13]. Our disk system at a density of $\phi = 0.85$ generally behaves elastically, keeping the same structures at depinning as in the moving phase, and we find that the PCA analysis gives distinctive results for this elastic state compared to the plastic flow phases that appear at lower densities. To probe the elastic system, it may be necessary to include features beyond mere structural measurements, such as the velocity of individual particles. This would provide additional information to the PCA that could allow it to discriminate different dynamic phases at the cost of significantly increasing the size of the feature vectors. Elastic depinning can occur for superconducting vortices or skyrmions interacting with weak pinning, or in the depinning of domain walls and elastic lines.

Another future direction is to apply PCA to other measures beyond the particle configurations, such as velocity fluctuations, the velocity-force curves, defect distributions, or local stress. Our results suggest that unsupervised machine learning can be a valuable method for identifying different nonequilibrium phases and the transitions between them. Since the data we employed in our analysis included site locations, a similar approach could be used for any type of particle-based system.

We note that in applying the PCA technique to off-lattice particle-based systems, some caution is in order. First of all, PCA will always return a result, but the result is not guaranteed to have a physical meaning. It is essential to scrutinize any learned correlations that appear in the data in order to compare with known physical symmetries before applying the method to study previously uncharacterized systems. PCA assumes that the physical features can be represented using a linear combination of perpendicular basis vectors. Given that many particle systems interact via nonlinear potentials, nonlinear machine learning techniques such as supervised discriminatory techniques that work well for facial identification algorithms may also be well suited for phase identification. For example, the relatively noisy P_1 signal observed for the elastic depinning at $\phi = 0.85$ may become better resolved by using a nonlinear algorithm.

VI. SUMMARY

In summary, we have shown that PCA can be used to identify the depinning transition and different nonequilibrium flow phases in a driven system of disks with short-range interactions moving over quenched disorder in the form of randomly placed pinning sites. In this system, traditional methods used to characterize depinning, such as the velocity-force curve and the Voronoi tessellation, show only weak signatures of the different dynamic states. In contrast, the PCA produces pronounced signals at the transitions between the pinned state, the moving phase separated state, and the moving smectic state. Using PCA, we also find evidence for more subtle phase transitions such as a clustered pinned phase as well as a transition between an amorphous and a crystalline phase separated state. The PCA can detect the onset of the jammed state and exhibits different signatures for plastic versus elastic depinning. The PCA method can be used to search for additional features in previously studied depinning systems such as superconducting vortices, Wigner crystals, skyrmions, and charge density wave systems, as well as to identify novel nonequilibrium phases in particle-based systems.

ACKNOWLEDGMENTS

This work was supported by the US Department of Energy through the Los Alamos National Laboratory. Los Alamos National Laboratory is operated by Triad National Security, LLC, for the National Nuclear Security Administration of the US Department of Energy (Contract No. 892333218NCA000001). This research was supported in part by the M. J. Murdock Charitable Trust and the Notre Dame Center for Research Computing.

---

[1] H. Abdi and L. J. Williams, Principal component analysis, Comput. Stat. **2**, 433 (2010).

[2] J. Shlens, A tutorial on Principal Component Analysis, arXiv:1404.1100.

[3] B. A. McKinney, D. M. Reif, M. D. Ritchie, and J. H. Moore, Machine learning for detecting gene-gene interactions: A review, Appl. Bioinform. **5**, 77 (2006).

[4] R. Pang, B. J. Lansdell, and A. L. Fairhall, Dimensionality reduction in neuroscience, Curr. Biol. **26**, R656 (2016).

[5] C. Bishop, *Pattern Recognition and Machine Learning* (Springer-Verlag, New York, 2006).

[6] J. Carrasquilla and R. G. Melko, Machine learning phases of matter, Nat. Phys. **13**, 431 (2017).

[7] S. J. Wetzel, Unsupervised learning of phase transitions: From principal component analysis to variational autoencoders, Phys. Rev. E **96**, 022140 (2017).

[8] W. Hu, R. R. P. Singh, and R. T. Scalettar, Discovering phases, phase transitions, and crossovers through unsupervised machine learning: A critical examination, Phys. Rev. E **95**, 062122 (2017).

[9] L. Wang, Discovering phase transitions with unsupervised learning, Phys. Rev. B **94**, 195105 (2016).

[10] R. B. Jadrich, B. A. Lindquist, and T. M. Truskett, Unsupervised machine learning for detection of phase transitions in off-lattice systems. I. Foundations, J. Chem. Phys. **149**, 194109 (2018).

[11] R. B. Jadrich, B. A. Lindquist, W. D. Pineros, D. Banerjee, and T. M. Truskett, Unsupervised machine learning for detection of phase transitions in off-lattice systems. II. Applications, J. Chem. Phys. **149**, 194110 (2018).

[12] L. Corte, P. M. Chaikin, J. P. Gollub, and D. J. Pine, Random organization in periodically driven systems, Nat. Phys. **4**, 420 (2008).

[13] C. Reichhardt and C. J. Olson Reichhardt, Depinning and nonequilibrium dynamic phases of particle assemblies driven over random and ordered substrates: A review, Rep. Prog. Phys. **80**, 026501 (2017).

[14] S. Bhattacharya and M. J. Higgins, Dynamics of a Disordered Flux Line Lattice, Phys. Rev. Lett. **70**, 2617 (1993).

[15] A. E. Koshelev and V. M. Vinokur, Dynamic Melting of the Vortex Lattice, Phys. Rev. Lett. **73**, 3580 (1994).

[16] C. Reichhardt, C. J. Olson, and F. Nori, Dynamic Phases of Vortices in Superconductors with Periodic Pinning, Phys. Rev. Lett. **78**, 2648 (1997).

[17] C. J. Olson, C. Reichhardt, and F. Nori, Nonequilibrium Dynamic Phase Diagram for Vortex Lattices, Phys. Rev. Lett. **81**, 3757 (1998).

[18] A. B. Kolton, D. Domínguez, and N. Grønbech-Jensen, Hall Noise and Transverse Freezing in Driven Vortex Lattices, Phys. Rev. Lett. **83**, 3061 (1999).

[19] D. Atkinson, D. A. Allwood, G. Xiong, M. D. Cooke, C. C. Faulkner, and R. P. Cowburn, Magnetic domain-wall dynamics in a submicrometre ferromagnetic structure, Nat. Mater. **2**, 85 (2003).

[20] A. T. Paxson and K. K. Varanasi, Self-similarity of contact line depinning from textured surfaces, Nat. Commun. **4**, 1492 (2013).

[21] F. I. B. Williams, P. A. Wright, R. G. Clark, E. Y. Andrei, G. Deville, D. C. Glattli, O. Probst, B. Etienne, C. Dorin, C. T. Foxon, and J. J. Harris, Conduction Threshold and Pinning Frequency of Magnetically Induced Wigner Solid, Phys. Rev. Lett. **66**, 3285 (1991).

[22] M.-C. Cha and H. A. Fertig, Topological defects, orientational order, and depinning of the electron solid in a random potential, Phys. Rev. B **50**, 14368 (1994).

[23] C. Reichhardt, C. J. Olson, N. Grønbech-Jensen, and F. Nori, Moving Wigner Glasses and Smectics: Dynamics of Disordered Wigner Crystals, Phys. Rev. Lett. **86**, 4354 (2001).

[24] K. B. Cooper, J. P. Eisenstein, L. N. Pfeiffer, and K. W. West, Observation of Narrow-Band Noise Accompanying the Breakdown of Insulating States in High Landau Levels, Phys. Rev. Lett. **90**, 226803 (2003).

[25] C. Reichhardt, C. J. Olson Reichhardt, I. Martin, and A. R. Bishop, Dynamical Ordering of Driven Stripe Phases in Quenched Disorder, Phys. Rev. Lett. **90**, 026401 (2003).

[26] H. J. Zhao, V. R. Misko, and F. M. Peeters, Dynamics of self-organized driven particles with competing range interaction, Phys. Rev. E **88**, 022914 (2013).

[27] X. Wang, H. Fu, L. Du, X. Liu, P. Wang, L. N. Pfeiffer, K. W. West, R.-R. Du, and X. Lin, Depinning transition of bubble phases in a high Landau level, Phys. Rev. B **91**, 115301 (2015).

[28] P. Brussarski, S. Li, S. V. Kravchenko, A. A. Shashkin, and M. P. Sarachik, Transport evidence for a sliding two-dimensional quantum electron solid, Nat. Commun. **9**, 3803 (2018).

[29] T. Schulz, R. Ritz, A. Bauer, M. Halder, M. Wagner, C. Franz, C. Pfleiderer, K. Everschor, M. Garst, and A. Rosch, Emergent electrodynamics of skyrmions in a chiral magnet, Nat. Phys. **8**, 301 (2012).

[30] N. Nagaosa and Y. Tokura, Topological properties and dynamics of magnetic skyrmions, Nat. Nanotechnol. **8**, 899 (2013).

[31] C. Reichhardt, D. Ray, and C. J. Olson Reichhardt, Collective Transport Properties of Driven Skyrmions with Random Disorder, Phys. Rev. Lett. **114**, 217202 (2015).

[32] W. Jiang, X. Zhang, G. Yu, W. Zhang, X. Wang, M. B. Jungfleisch, J. E. Pearson, X. Cheng, O. Heinonen, K. L. Wang, Y. Zhou, A. Hoffmann, and S. G. E. te Velthuis, Direct observation of the skyrmion Hall effect, Nat. Phys. **13**, 162 (2017).

[33] W. Legrand, D. Maccariello, N. Reyren, K. Garcia, C. Moutafis, C. Moreau-Luchaire, S. Collin, K. Bouzehouane, V. Cros, and A. Fert, Room-temperature current-induced generation and motion of sub-100 nm skyrmions, Nano Lett. **17**, 2703 (2017).

[34] S. A. Díaz, C. J. O. Reichhardt, D. P. Arovas, A. Saxena, and C. Reichhardt, Fluctuations and noise signatures of driven magnetic skyrmions, Phys. Rev. B **96**, 085106 (2017).

[35] G. Grüner, The dynamics of charge-density waves, Rev. Mod. Phys. **60**, 1129 (1988).

[36] C. R. Myers and J. P. Sethna, Collective dynamics in a model of sliding charge-density waves. I. critical behavior, Phys. Rev. B **47**, 11171 (1993).

[37] Y. Li, S. G. Lemay, J. H. Price, K. Cicak, K. O'Neill, K. Ringland, K. D. Finkelstein, J. D. Brock, and R. E. Thorne, Imaging Shear in Sliding Charge-Density Waves by X-Ray Diffraction Topography, Phys. Rev. Lett. **83**, 3514 (1999).

[38] C. Reichhardt and C. J. Olson, Colloidal Dynamics on Disordered Substrates, Phys. Rev. Lett. **89**, 078301 (2002).

[39] A. Pertsinidis and X. S. Ling, Statics and Dynamics of 2D Colloidal Crystals in a Random Pinning Potential, Phys. Rev. Lett. **100**, 028303 (2008).

[40] P. Tierno, Depinning and Collective Dynamics of Magnetically Driven Colloidal Monolayers, Phys. Rev. Lett. **109**, 198304 (2012).

[41] T. Bohlein, J. Mikhael, and C. Bechinger, Observation of kinks and antikinks in colloidal monolayers driven across ordered surfaces, Nat. Mater. **11**, 126 (2012).

[42] A. Vanossi, N. Manini, and E. Tosatti, Static and dynamic friction in sliding colloidal monolayers, Proc. Natl. Acad. Sci. USA **109**, 16429 (2012).

[43] D. McDermott, J. Amelang, C. J. Olson Reichhardt, and C. Reichhardt, Dynamic regimes for driven colloidal particles on a periodic substrate at commensurate and incommensurate fillings, Phys. Rev. E **88**, 062301 (2013).

[44] C. J. Olson Reichhardt, E. Groopman, Z. Nussinov, and C. Reichhardt, Jamming in systems with quenched disorder, Phys. Rev. E **86**, 061301 (2012).

[45] A. L. Graves, S. Nashed, E. Padgett, C. P. Goodrich, A. J. Liu, and J. P. Sethna, Pinning Susceptibility: The Effect of Dilute, Quenched Disorder on Jamming, Phys. Rev. Lett. **116**, 235501 (2016).

[46] D. Cule and T. Hwa, Tribology of Sliding Elastic Media, Phys. Rev. Lett. **77**, 278 (1996).

[47] J. Tekić, O. M. Braun, and B. Hu, Dynamic phases in the two-dimensional underdamped driven Frenkel-Kontorova model, Phys. Rev. E **71**, 026104 (2005).

[48] A. Vanossi, N. Manini, M. Urbakh, S. Zapperi, and E. Tosatti, Colloquium: Modeling friction: From nanoscale to mesoscale, Rev. Mod. Phys. **85**, 529 (2013).

[49] J. M. Carlson and J. S. Langer, Properties of Earthquakes Generated by Fault Dynamics, Phys. Rev. Lett. **62**, 2632 (1989).

[50] M.-C. Miguel, A. Vespignani, M. Zaiser, and S. Zapperi, Dislocation Jamming and Andrade Creep, Phys. Rev. Lett. **89**, 165501 (2002).

[51] C. Zhou, C. Reichhardt, C. J. O. Reichhardt, and I. J. Beyerlein, Dynamic phases, pinning, and pattern formation for driven dislocation assemblies, Sci. Rep. **5**, 8000 (2015).

[52] A. Sengupta, S. Sengupta, and G. I. Menon, Driven disordered polymorphic solids: Phases and phase transitions, dynamical coexistence and peak effect anomalies, Phys. Rev. B **81**, 144521 (2010).

[53] A. Morin, N. Desreumaux, J.-B. Caussin, and D. Bartolo, Distortion and destruction of colloidal flocks in disordered environments, Nat. Phys. **13**, 63 (2017).

[54] Cs. Sándor, A. Libál, C. Reichhardt, and C. J. Olson Reichhardt, Dynamic phases of active matter systems with quenched disorder, Phys. Rev. E **95**, 032606 (2017).

[55] P. Le Doussal and T. Giamarchi, Moving glass theory of driven lattices with disorder, Phys. Rev. B **57**, 11356 (1998).

[56] L. Balents, M. C. Marchetti, and L. Radzihovsky, Nonequilibrium steady states of driven periodic media, Phys. Rev. B **57**, 7705 (1998).

[57] F. Pardo, F. de la Cruz, P. L. Gammel, E. Bucher, and D. J. Bishop, Observation of smectic and moving-Bragg-glass phases in flowing vortex lattices, Nature (London) **396**, 348 (1998).

[58] L. Li, Y. Yang, D. Zhang, Z. Ye, S. Jesse, S. V. Kalinin, and R. K. Vasudevan, Machine learning-enabled identification of material phase transitions based on experimental data: Exploring collective dynamics in ferroelectric relaxors, Sci. Adv. **4**, eaap8672 (2018).

[59] Y. Yang, D. McDermott, C. J. Olson Reichhardt, and C. Reichhardt, Dynamic phases, clustering, and chain formation for driven disk systems in the presence of quenched disorder, Phys. Rev. E **95**, 042902 (2017).

[60] F. Pedregosa, G. Varoquaux, A. Gramfort, V. Michel, B. Thirion, O. Grisel, M. Blondel, P. Prettenhofer, R. Weiss, V. Dubourg, J. Vanderplas, A. Passos, D. Cournapeau, M. Brucher, M. Perrot, and E. Duchesnay, Scikit-learn: Machine learning in Python, J. Mach. Learn. Res. **12**, 2825 (2011).